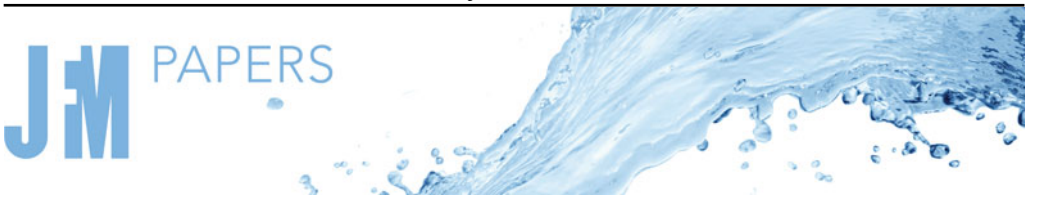
J. Fluid Mech. (2026), *vol.* 1042, A23, doi:10.1017/jfm.2026.11975



Enhanced ionic diffusion by intrinsic liquid–gas slippage

Meng Yan[1] **and Yanbo Xie**[2]

[1]School of Physical Science and Technology, Northwestern Polytechnical University, Xi'an 710072, PR China

[2]School of Aeronautics and Institute of Extreme Mechanics, Northwestern Polytechnical University, Xi'an 710072, PR China

Corresponding author: Yanbo Xie, ybxie@nwpu.edu.cn

(Received 18 August 2025 UTC; revised 28 April 2026 UTC; accepted 22 July 2026 UTC)

Transport phenomena at liquid–gas interfaces remain not fully understood, particularly due to creating reproducible surfaces to quantify intrinsic slip and enhanced mass transport. Here we measure ionic diffusion currents across a bubble liquid film bounded by solid–liquid–gas interfaces under controlled salt gradients and surfactant concentrations. Ionic surfactant adsorption significantly increases the diffusion current, which peaks at 10^{-1} mM and decreases at higher concentrations. We attribute this non-monotonic behaviour to two competing effects: increased surface charge density and reduced slip length induced by surfactant adsorption. We develop an analytical theory for diffusion currents with slip boundaries, enabling extraction of the effective surface charge density and intrinsic slip length as functions of surfactant concentration. The effective slip length remains $\sim 3\,\mu$m below a critical surfactant concentration but drops sharply above 10^{-2} mM. These results establish a quantitative framework for slip-enhanced electrokinetic transport at surfactant-covered liquid–gas interfaces.

Key words: electrokinetic flows, microscale transport, thin films

1. Introduction

Boundary slip is critical for the interfacial flow and transport phenomena in micro-/nanofluidics (Sparreboom *et al.* 2009; Qin *et al.* 2011; Secchi *et al.* 2016; Cai *et al.* 2025), and has been widely used in drag reduction (Huang *et al.* 2019; Li *et al.* 2020*b*; Wang *et al.* 2022), energy harvesting (Rankin & Huang 2016; Long *et al.* 2020) and efficient lubrication (Aurelian *et al.* 2011; Yan *et al.* 2024). The observation of boundary slip can be traced back to the time of Leonardo da Vinci (Xia 2024), and Navier introduced the slip length b to quantitatively describe the slippage (Navier 1822).

© The Author(s), 2026. Published by Cambridge University Press.

https://doi.org/10.1017/jfm.2026.11975 Published online by Cambridge University Press

Apparent boundary slip has been observed on hydrophobic surfaces (Feuillebois *et al.* 2009; Rothstein 2010), where the slip length correlates with the contact angle of the solid surface (Ou *et al.* 2004; Davies *et al.* 2006; Huang *et al.* 2008; Bouzigues *et al.* 2008; Lee & Kim 2014). The obvious slip at the hydrophobic surfaces has been attributed to the presence of surface bubbles, which strongly reduce the solid–liquid (SL) friction since the gas phase is shear-free due to the negligible viscosity of air (Tyrrell & Attard 2001; Lauga & Stone 2003; Haase *et al.* 2016). Interfaces covered by surface bubbles have considerable potential for surface cleaning (Liu & Craig 2009), flotation (Wu *et al.* 2012) and nanomaterial engineering (Berkelaar *et al.* 2013). Another widely used approach is to trap air pockets within microstructured surfaces on hydrophobic surfaces (Choi *et al.* 2006; Ming *et al.* 2011). These gas cavities, stabilised by Laplace pressure, form macroscale liquid–gas (LG) interfaces that significantly reduce drag and promote interfacial transport (Feuillebois *et al.* 2009; Karatay *et al.* 2013; Lee *et al.* 2014*b*).

Thus, maximising the bubble area at a surface could help to enhance the flow and transport phenomena in confinement according to previous studies. Besides, precise measurement of the LG interface slippage is crucial to understanding the relevant transport phenomena. Over the past few decades, various experimental techniques have been developed to characterise the slip properties of LG interfaces (Lee *et al.* 2016), including particle image velocimetry (Bouzigues *et al.* 2008; Li *et al.* 2020*a*), atomic force microscopy (Nizkaya *et al.* 2016), capillary techniques (Lohse & Zhang 2015) and rheometry (Choi & Kim 2006; Truesdell *et al.* 2006; Lee *et al.* 2008). However, device-to-device differences often result in large variations in the measured slip length. For instance, the flow profile in a hydrophobic microchannel shows an apparent slip velocity at the solid boundary, with micro-particle image velocimetry measurements indicating slip lengths of the order of tens of nanometres (Bouzigues *et al.* 2008), while Lee *et al.* reported a giant slip length of 185 μm by controlling the pitch and gas fraction on a hydrophobic surface using a rheometer system (Lee *et al.* 2008).

These inconsistencies arise from two primary challenges. First, the stochastic formation of surface bubbles is difficult to control (Zhang *et al.* 2013; Lohse & Zhang 2015), resulting in variations of experimental results in interfacial properties such as contact angle, surface roughness and curvature-dependent surface tension (Seddon & Lohse 2011; An *et al.* 2015). This heterogeneity in surface chemistry causes uncertainties in slip length measurements and hinders reliable electrokinetic analysis (Haase *et al.* 2016; Li *et al.* 2016; Verschoof *et al.* 2016). Haase *et al.* (2016) found that the effective slip length over a bubble mattress reaches a maximum at a small protrusion angle ($\sim 9°$), while Li *et al.* (2016) reported that the slip length increased from 8 to 512 nm as the nanobubble coverage increased from 1.7 % to 50.8 %, while contact angle decreased from 42.8° to 16.6°.

Second, for trapped air pockets in micro- and nanoscale surface structures, boundary slip is highly sensitive to the geometry and physicochemical properties of the SL interface, including surface topography (Ou *et al.* 2004; Davies *et al.* 2006), wettability (Wang *et al.* 2009; Lee & Kim 2014) and the gas fraction retained in surface features (Lee *et al.* 2008; Hu *et al.* 2018). In addition, external perturbations such as pressure (Lv *et al.* 2014), air diffusion (Bobji *et al.* 2009; Poetes *et al.* 2010) and evaporation (Reyssat *et al.* 2008; Tsai *et al.* 2010) can destabilise the LG interface by overcoming the energy barrier, thereby degrading the slip effect (Lv *et al.* 2016). For instance, Karatay *et al.* used microcavities in a microfluidic channel to trap microbubbles and found that the effective slip length reached a maximum at an optimal protrusion angle around 10°, leading to drag reduction of up to 23 %. However, beyond a critical angle ($\sim 62°$), the slip length became negative, indicating increased flow resistance (Karatay *et al.* 2013). Lee & Kim (2014) also showed that significant slip only occurred on surfaces with short, sparsely distributed and strongly

https://doi.org/10.1017/jfm.2026.11975 Published online by Cambridge University Press

hydrophobic protrusions. Moreover, Lv *et al.* (2014) demonstrated that shear stress could deform air pockets and alter their stability, and that high operating pressures tend to collapse the pockets and suppress interfacial slip. These findings highlight the necessity for a platform that can characterise the intrinsic slip behaviour of LG interfaces under shear-free, stable and reproducible conditions.

In this work, we investigate the ionic diffusion currents through a static bubble thin liquid film with a solid–liquid–gas interface, uncovering the slip-amplified effective surface charge density and intrinsic slip length at the LG interface under the influence of ionic surfactants. Unlike pressure-driven flow, the liquid-film thickness remains constant under diffusio-osmosis, with a known and reproducible LG interface. We introduced a single microbubble in a circular glass capillary, forming a thin liquid film between the bubble and the capillary wall (Ma *et al.* 2020; Niu *et al.* 2024). Under a wide range of salt concentration gradients across the bubble in various surfactant concentrations, we measured the conductance and diffusion currents.

Our results show the effective surface charge density at the LG interface increases with surfactant concentration and reaches a maximum near 10^{-1} mM, then decreases at higher concentrations. We attribute the initial increase to enhanced intrinsic surface charge from adsorbed surfactants, and the subsequent decrease to increased interfacial friction at high adsorption density, consistent with our theoretical analysis and prior molecular simulations (Joly *et al.* 2014; Yan *et al.* 2025).

We develop an analytical model based on adsorption isotherms and Marangoni stress to quantify surfactant-induced variations in slip length at the LG interface. The model captures diffusion currents under osmotic driving and enables extraction of the intrinsic slip length as a function of surfactant concentration. The slip length remains approximately 3 μm below 10^{-2} mM and decreases sharply at higher concentrations. By maximising the LG interfacial area using a confined bubble, we significantly enhance flow and mass transport within the film nanochannel. This configuration increases osmotic energy conversion compared with non-slipping solid interfaces and provides a strategy to exploit soft, slipping boundaries to boost nanoscale transport.

2. Experimental set-up

Figure 1(*a*) illustrates the experimental set-up. A circular glass capillary is embedded in a polydimethylsiloxane (PDMS) microfluidic chip fabricated by standard photolithography. A rectangular PDMS microchannel (200 μm wide, 400 μm high) serves as both a loading chamber and a connection port, enabling gas and electrolyte injection, inserting two Ag/AgCl electrodes, and rapid solution exchange to establish the salt concentration gradient across the bubble. We manually generated a single microbubble by injecting nitrogen gas (99.99 %) into the microchannels by using a syringe pump. Consequently, we guided the bubble into the circular glass capillary (300 μm inner diameter). The microbubble occupies most of the capillary cross-section, leaving a thin liquid film between the bubble and the capillary wall (figure 1*b*).

The bubble size remains constant over 12 h, due to the low solubility of nitrogen gas in water. As previously reported (Ma *et al.* 2020), the film thickness in equilibrium state is governed by the balance between the Laplace pressure of the bubble meniscus and the disjoining pressure of the thin liquid film, considering van der Waals force, electrostatic repulsion between interfaces and surface wettability. We pretreated the glass capillary by sequentially injecting 30 % hydrogen peroxide and 100 mM sodium hydroxide for 30 and 60 minutes, respectively. We then rinsed the capillary with NaCl solution for at least 30 minutes. To measure the ionic diffusion current, we established a salt concentration

https://doi.org/10.1017/jfm.2026.11975 Published online by Cambridge University Press

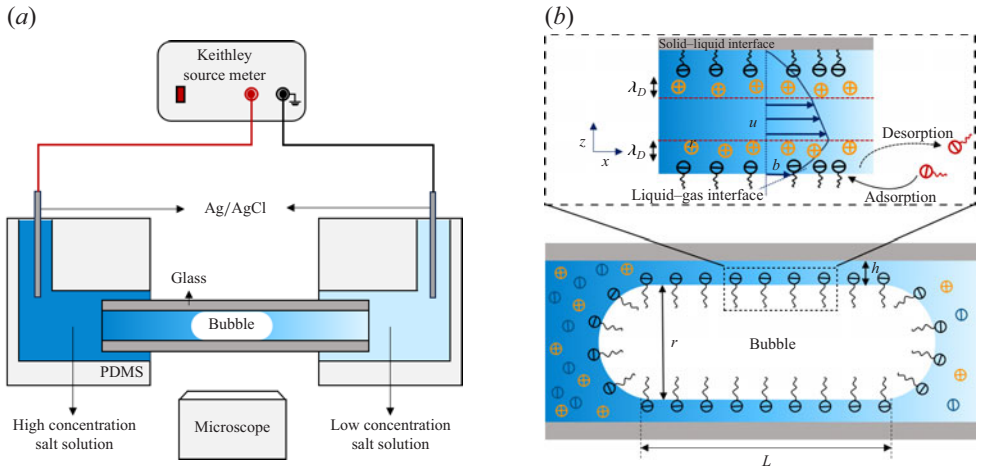


Figure 1. Schematic of the experimental set-up. (*a*) Experimental set-up includes a bubble control system, microscope optical imaging system and electrical measurement system. (*b*) Geometry in the region of the LG interface in detail.

gradient across the bubble. First, we filled the microchannels and generated a bubble using a low-concentration solution ($C_{min} = 1$ mM). We then injected a high-concentration solution (C_{max}) from the left-hand side to push the bubble into the capillary and establish the concentration gradient. We varied C_{max} from 10 to 200 mM for current measurements.

We measured the conductance of the bubble liquid film using both triangular voltage sweeps and electrochemical impedance spectroscopy (EIS) (Li *et al.* 2025), enabling us to infer the film thickness from its conductance in NaCl solution. We applied a triangular voltage sweep (± 0.5 V) within the electrochemical window to avoid concentration polarisation and limiting-current effects (Schoch *et al.* 2008). A Keithley 6430 source meter generated the waveform at a quasi-static scan frequency of ~ 0.435 Hz. The measured response remained in the resistive regime below ~ 100 Hz, thus avoiding the capacitive effects as indicated by EIS results.

The EIS was performed with a CH Instruments 600E electrochemical workstation. Two Ag/AgCl electrodes were inserted into side ports of the PDMS chip (figure 1*a*) to complete the measurement circuit. We first characterised the electrical resistance of the system without a bubble (R_{nb}), and then measured the resistance after introducing a bubble (R_b). This resistance change enabled us to derive the electrical resistance of the film nanochannel as $R_f = R_b - R_{nb}$. The resistance of the bubble meniscus is much smaller than that of the bubble liquid film; thus, we could estimate the liquid film resistance from the resistance deviation with and without the bubble in the above approach (Ma *et al.* 2020).

To evaluate surfactant effects, we changed the sodium dodecylsulphate (SDS) concentration, C_{SDS}, from 0 to 1 mM. At each C_{SDS}, we measured the diffusion current under a series of NaCl concentration gradients across the bubble. Because the diffusion current scales linearly with the logarithm of the concentration ratio, $\ln(C_{max}/C_{min})$, we extracted the effective surface charge density from the slope. In all measurements, we fixed the right-hand reservoir at $C_{min} = 1$ mM and varied the left-hand reservoir concentration C_{max}. After each run, we flushed the device sequentially with H_2O_2, NaOH and NaCl solutions to remove residual surfactants and ions. All experiments were conducted at pH 9 using freshly prepared solutions with ultrapure water (18.2 MΩ cm).

https://doi.org/10.1017/jfm.2026.11975 Published online by Cambridge University Press

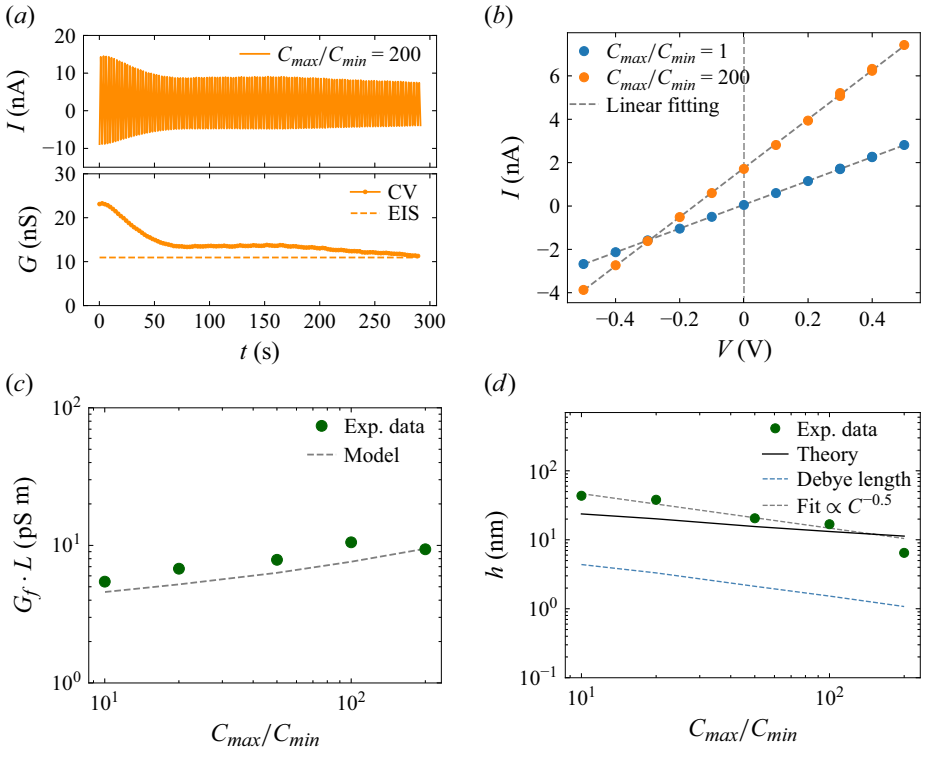


Figure 2. The electrical characterisation of the film nanochannel. (*a*) The CV measurements at a salt concentration ratio of 200 show time-dependent decay of nanochannel conductance magnitude (top). System conductance evolution from CV (solid curves) converges towards EIS baseline values (dashed) over time (bottom). (*b*) Typical *I*–*V* curves at the saturated states at salt concentration ratios of 1 (blue circles) and 200 (orange circles) show the Ohmic behaviour of the system. The dashed line represents a linear fit. (*c*) Nanochannel conductance per unit length across tested conditions (green circles), with theoretical predictions (black dashed line). (*d*) Normalised conductance-derived film thickness (green circles) versus salt concentration ratio at pH 9. The solid line shows the theoretical value of film thickness. The blue dashed line is the Debye length and the black dashed line shows the scaling law for the film thickness.

3. Experimental results

3.1. *Ionic conduction*

Typical results for the bubble film under a sweeping voltage are shown in figure 2(*a*, top), with 200 mM NaCl solution on the left and 1 mM NaCl solution on the right-hand side of the bubble. By linear fitting of the $I-V$ curves, we obtained the system conductance decreasing gradually over successive scanning cycles (figure 2*a*, bottom), and finally reaching a saturated value. We could observe such a reduction in all of our electrical measurements for the beginning scanning cycles. We attribute the initial reduction and saturation of the bubble film conductance to the drainage of trapped water within the film. As the electro-osmotic flow induced by the scanning voltage drains this excess water trapped in the film, the film thins until it stabilises at a constant equilibrium thickness. This thickness is determined by the balance between capillary and disjoining pressures (Ma *et al.* 2020; Niu & Xie 2025). The results show that the saturated conductance obtained by EIS is in agreement with that determined by cyclic voltammetry (CV) (figure 2*a*, bottom).

https://doi.org/10.1017/jfm.2026.11975 Published online by Cambridge University Press

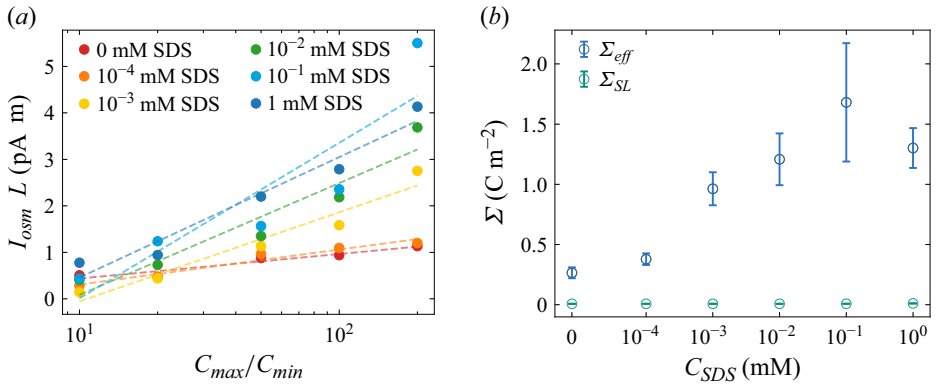


Figure 3. (*a*) Diffusion current per unit length at different SDS concentrations. (*b*) The effective charge density at the gas–solid–liquid interface (blue open circles) from diffusion current measurements at a salt concentration of 1 mM, and at the SL interface (green open circles) from electrokinetic current measurements.

We analysed the saturated conductance extracted from the $I-V$ curves (figure 2*b*). Blue data points in figure 2(*b*) represent the results under symmetric (1 mM NaCl) concentration electrolyte solution filled on both sides, while the orange points were obtained under asymmetric concentration conditions with 1 mM NaCl filled in the right and 200 mM in the left reservoir. By linear fitting (dashed lines), we determined the film conductance in both conditions. A net current was found at $V = 0$ under a concentration gradient confirming a diffusion current across the bubble film, with the average value over the last ten consecutive cycles after the system reached a steady state.

To eliminate the variations of bubble length in each measurement, we evaluated the length-corrected conductance from the I–V slopes (figure 2*c*). The corrected conductance ($G_f L$, with L denoting the bubble length) increased with the salt concentration ratio but decreased at the highest ratio, likely due to film thinning at high ionic strength.

3.2. *Diffusion current measurement*

Introducing a higher salt concentration on the left-hand side of the capillary than that on the right-hand side (1 mM NaCl) produced a net current at zero bias ($V = 0$), driven by a chemical potential gradient across the bubble (Fair & Osterle 1971). This diffusion current reflects ion selectivity within the electric double layers (EDLs) at the LG and SL interfaces. Counterions dominate both the charge transport and the diffusio-osmotic flow within the bubble film.

We fixed the salt concentration in the right-hand reservoir ($C_{min} = 1$ mM) and varied the left-side concentration (C_{max}) from 10 to 200 mM to probe the effect of the salt gradient on diffusion current and conductance. Similar to the conductance, to account for variations in bubble length, we normalised the measured diffusion current by the film length ($I_{sys}L$), enabling consistent comparison across experiments. As shown in figure 3(*a*), the normalised diffusion current (red circles) increases linearly with $\ln(C_{max}/C_{min})$.

Surfactants play a crucial role in determining the slip length at the LG interface and the zeta potential (Joly *et al.* 2014), significantly affecting electrokinetic phenomena, even at trace amounts (Peaudecerf *et al.* 2017; Landel *et al.* 2020). Therefore, investigating the impact of surfactant concentration on zeta potential and slip boundaries via diffusion current is important. Here, we gradually changed the SDS concentration (C_{SDS}) from 0 to 1 mM, while keeping the concentration gradient of NaCl solution across the bubble as a constant ($C = 1$ mM). As shown in figure 3(*a*), the normalised diffusion current remains

https://doi.org/10.1017/jfm.2026.11975 Published online by Cambridge University Press

proportional to $\ln(C_{max}/C_{min})$, in different slopes as C_{SDS} varies. This change is likely due to the variation in surface charge density caused by the adsorption of ionic surfactants (SDS), which we analyse below.

4. Theoretical analysis

In this section, we analytically calculate the effective surface charge density and effective slip length at the LG interface. We first determine the film thickness from conduction which we found is larger than the Debye length, as shown in figure 2(*d*), which indicates the diffusion current can be calculated within the Debye length, instead of film thickness. Then, we derive an effective surface charge density of the liquid-film system ($\Sigma_{eff} = \Sigma_{LG}^{eff} + \Sigma_{SL}$) from the measured diffusion current, including the contribution from LG and SL interfaces. By streaming current measurements, we characterised the surface charge density at the SL interface Σ_{SL}. Therefore, we can derive the effective surface charge density at the LG interface Σ_{LG}^{eff} by deduction of Σ_{SL} from the liquid-film system (§§ 2 and 3). Finally, we could estimate the slip length at the LG interface using the isotherm adsorption of surfactants, in various surfactant concentrations (§ 4).

4.1. *Ionic conduction and film thickness*

The effective film thickness h is calculated from conduction measurements. Under a salt-concentration gradient, we treat the liquid resistance as series connection of infinitesimal resistors. Thus, the resistance can be expressed by

$$R_f = \frac{1}{G_f} = \int_0^L \frac{\mathrm{d}x}{2\pi r h\,[k_b(C(x)) + k_s(C(x))]}, \tag{4.1}$$

where r is the bubble radius of the glass capillary. Here, the thickness obtained from (4.1) is interpreted as an effective film thickness derived from the measured conductance, rather than a local thickness profile $h(x)$. The bulk conductivity of electrolytes solution (Appendix C, table 2) is a function of axis position $C(x)$ considering the salt gradient. To describe the axial salt transport in the film under finite advection, we consider the one-dimensional steady advection–diffusion equation with averaged velocity u and diffusivity D. The axial concentration field then satisfies the diffusion–convection equation (Lee *et al.* 2014*a*)

$$D\frac{\mathrm{d}^2C}{\mathrm{d}x^2} - u\frac{\mathrm{d}C}{\mathrm{d}x} = 0. \tag{4.2}$$

With boundary condition of $C(0) = C_{max}$ and $C(L) = C_{min}$, we obtain

$$C(x) = C_{max} + (C_{min} - C_{max})\frac{\exp(Pe \cdot x/L) - 1}{\exp(Pe) - 1}, \tag{4.3}$$

where $Pe = uL/D$. The Péclet numbers in our experiments are listed in table 3 of Appendix C and range from 0.05 to 1.25, where the maximum value occurs in the surfactant-free conditions at the largest salinity gradient. The concentration profile comes to the linear distribution when limit $Pe \ll 1$.

Considering the surface conductivity arising from the EDLs at both LG and SL interfaces, we have (Levine *et al.* 1975)

$$k_s(C) = \frac{\mu\,(\Sigma_{LG}(C) + \Sigma_{SL}(C))}{h}\left(1 + \frac{e}{2\pi\ell_B\mu\eta}\right), \tag{4.4}$$

https://doi.org/10.1017/jfm.2026.11975 Published online by Cambridge University Press

where μ, ℓ_B, e and η are the counterion mobility, Bjerrum length, elementary charge and viscosity, respectively.

We fitted the zeta potential at various salt concentrations (see Appendix C, table 4) for surfactant-free LG interface (ζ_{LG}) and SL interface (ζ_{SL}) based on our previous experimental data (Ma *et al.* 2020), obtaining

$$\zeta_{LG}(C) = 4.34\ \ln(C - 0.0019) - 45.2 \quad (\text{mV}), \tag{4.5}$$

$$\zeta_{SL}(C) = 14.9\ \ln(C + 0.420) - 104 \quad (\text{mV}). \tag{4.6}$$

We take the Grahame relation to connect the surface potential to surface charge densities, which are later used in the surface conduction term in (4.4). Here, the LG zeta potential ζ_{LG} denotes the zeta potential at the LG interface that is used for film thickness calculation. The effective film thickness can be obtained by substituting the bulk conductivity and surface conductivity equation (4.4) into (4.1).

Given the measured G_f, we solve (4.1) numerically and obtain a thickness h across a broad range of salt concentrations (green circles in figure 2*d*). The results show that the film thickness $h \propto C^{-0.5}$ (dashed line in figure 2*d*), consistent with our previous studies (Ma *et al.* 2020).

The conductance-based film thickness obtained from (4.1)–(4.6) is shown as the circles in figure 2(*d*). We examine the film thickness by force balance between capillary pressure p_c and disjoining pressure Π_d under the salt-gradient conditions, for which theoretical film thickness changes with salt concentration. In a surfactant-free NaCl solution system, we use the DLVO description and consider the disjoining pressure Π_d including the contribution from the van der Waals term Π_{vdW} and the electrostatic term Π_{el}. Since the salt concentration changes along the film axis, the electrostatic term was averaged along the axial direction of the film. The force balance $p_c = \Pi_d$ is therefore written as follows:

$$p_c = \Pi_{vdW}(h) + \frac{1}{L}\int_0^L \Pi_{el}\,\mathrm{d}x. \tag{4.7}$$

Capillary pressure of the bubble meniscus is given by $p_c = 2\gamma\cos\alpha/r$, where γ and α are the interfacial tension and apparent wetting angle of the bubble, respectively. Here, we have approximated the curvature radius as the capillary radius r, since the film thickness h is negligible compared with the capillary radius. The apparent wetting angle of the bubble was optically measured in the capillary using image analysis software (drop shape analysis), yielding a value of 15°. The van der Waals pressure is $\Pi_{vdW} = -A/6\pi h^3$, where A is the Hamaker constant for the fused silica–water–air system, reported as $A = -1.03 \times 10^{-20}$ J (Hough & White 1980). The electrostatic repulsion is $\Pi_{el}(C(x)) = 64k_BTn_\infty\Gamma_1(C(x))\Gamma_2(C(x))\exp(-h/\lambda_D)$ (Ma *et al.* 2020), where Γ_1 and Γ_2 are the dimensionless surface potentials at the LG and SL interfaces. These surface potentials Γ_i are related to the corresponding zeta potentials ζ_i by $\Gamma_i = \tanh(ze\zeta_i/4k_BT)$, where $i = 1, 2$. Here z, k_B, T and n_∞ are the ion valence, Boltzmann constant, temperature and bulk number density of the electrolyte ions, respectively, and λ_D represents the Debye length. The physical constants used in the calculations are listed in table 1 of Appendix C.

Due to the force balance between Laplace pressure and disjoining pressure, we determine the theoretical film thickness numerically under the salt-gradient conditions (black solid line in figure 2*d*). The corresponding Debye length, defined as the axial average of the local Debye length λ_D, is shown by the dashed line in figure 2(*d*), where we have $h/\lambda_D \approx 3{-}5.75$ in all probed concentrations, resulting in a thin EDL approximation. The surface potential drops to less than 5 % at the centre of the liquid film.

https://doi.org/10.1017/jfm.2026.11975 Published online by Cambridge University Press

4.2. *Diffusion current*

The osmotic pressure drives the diffusion of counterions, as well as the diffusio-osmotic flow within the EDLs, generating an electric current, which has been known since the work of Fair & Osterle (1971). The diffusion term can be written as $I_D = 2\pi r \int_0^h \mathrm{d}z\, e(j_{D,+} - j_{D,-})$, where $j_{D,\pm} = -D_s \nabla C_\pm$ denotes the diffusive flux of cations/anions. For a symmetric electrolyte (assuming $D_+ \approx D_- = D_s$), the net diffusion current across the channel can be approximated as $I_D = 2\pi r D_s \partial_x \Sigma \approx 2\pi r D_s(\Sigma(C_{max}) - \Sigma(C_{min}))/L$ (Siria *et al.* 2013). Since the surface charge density may be changed by the salt concentration (Najafi *et al.* 2007), here we estimate the diffusion term. Under the largest salt concentration gradient (200 mM^{-1} mM), we found that the diffusion term caused by surface charge density gradient has only 2 % contribution in the system, by taking $\Sigma(C_{max}) = -0.0234\ \mathrm{C\,m^{-2}}$, $\Sigma(C_{min}) = -0.0037\ \mathrm{C\,m^{-2}}$, $L = 656\ \mu\mathrm{m}$ and $D_s = 1.33 \times 10^{-9}\ \mathrm{m^2\,s^{-1}}$ in the above calculation. Thus, the small contribution from the diffusion term arises from small surface charge density gradient, enabling us to make a constant charge density assumption along the axis of the liquid film for simplicity.

As a result, the measured diffusion current I_{sys} arises from the diffusio-osmotic flow which drives counterion diffusion within the EDL of both SL (I_{SL}) and LG (I_{LG}) interfaces. We define the diffusion current I_i at either interface i (SL or LG) as

$$I_i = 2\pi r \int_{film} e(C_+ - C_-)u_i(z)\,\mathrm{d}z. \tag{4.8}$$

To evaluate integral (4.8), we must derive the expression of flow velocity $u_i(z)$ at both LG and SL interfaces.

4.3. *Diffusio-osmotic flow*

Our liquid-film channel is considered as a two-dimensional slit system with a (upper) SL and (lower) LG interface, as shown in figure 2(*b*). The LG interface is treated as a Navier slip boundary with slip velocity $u_{slip} = b(\partial u/\partial z)|_{z=0}$, while the SL interface at the capillary wall is treated as a no-slip boundary ($u|_{z=h} = 0$).

Moreover, even if a weak diffusio-osmotic convection exists, it still has a minor effect on the ion distribution compared with the EDL within the liquid film. In our experiments, the bubble length ($\sim$1 mm scale) is much larger than the liquid film thickness ($h \sim 10$ nm range). Thus, the axial potential caused by external bias is much weaker than the transverse one caused by the EDL ($\partial^2\phi/\partial x^2 \ll \partial^2\phi/\partial z^2$). Therefore, we still can approximate the counterion distribution by classical EDL theories, and the convection only provides a higher-order (minor) correction to the axial profile $C(x)$ (Prieve *et al.* 1984):

$$C_\pm(x, z) = C_\infty(x)\exp(\mp\Phi(z)), \tag{4.9}$$

where $C_+(x, z)$ and $C_-(x, z)$ denote the density of positive and negative ions near the charged surface, respectively, and $\Phi = e\phi/k_BT$ is the surface potential ϕ normalised by thermal energy k_BT.

The diffusio-osmotic velocity in the liquid film $\boldsymbol{u}$ is determined by the Stokes equation:

$$\eta\nabla^2\boldsymbol{u} - \nabla P + e(C_+ - C_-)(-\nabla\psi) = 0, \tag{4.10}$$

where P is the pressures inside of the liquid film including the disjoining pressures between SL and LG interfaces as the normal vector and the osmotic pressure gradient across the bubble as the parallel factor. We may derive the pressure P by integrating the z component of (4.10) using (4.9) for the ion distributions:

$$P(x, z) = P_\infty + 2k_BTC_\infty(x)[\cosh(\Phi(z)) - 1]. \tag{4.11}$$

https://doi.org/10.1017/jfm.2026.11975 Published online by Cambridge University Press

Substituting (4.11) into the x component of (4.10), the diffusio-osmotic velocity profile can be written as

$$\eta \frac{\mathrm{d}^2 u}{\mathrm{d}z^2} = 2k_B T\,[\cosh \Phi(z) - 1]\,\frac{\mathrm{d}C_\infty}{\mathrm{d}x}. \tag{4.12}$$

In the liquid-film nanochannel, the microbubble surface is modelled as the LG interface, which defines the inner boundary of the film at $z = 0$, while the outer boundary at $z = h$ is the SL interface. We impose no-slip condition at the SL interface, $u(h) = 0$, and a Navier slip condition at the LG interface. We first consider the diffusion-driven flow with interfacial slip, for which the slip velocity obeys

$$u_{slip} = b \frac{\partial u}{\partial z}\Big|_{z=0}, \tag{4.13}$$

where b is the slip length and u_{slip} is the slip velocity at the LG interface, incorporating the influence of the Marangoni effect. By integrating (4.12) along the z direction, and taking the boundary condition (4.13), we obtain the slip velocity at the LG interface under diffusio-osmosis:

$$u_{slip} = -b \frac{2k_B T}{\eta} \left[\int_0^{h/2} [\cosh \Phi(z) - 1]\ \mathrm{d}z \right] \frac{\mathrm{d}C_\infty}{\mathrm{d}x}. \tag{4.14}$$

Using the thin EDL approximation, the integral can be evaluated analytically to leading order. Using the identity $\mathrm{d}z = -\mathrm{d}\Phi/(\kappa\sqrt{2(\cosh \Phi - 1)})$ derived from the Poisson–Boltzmann equation, the integral term becomes (Mouterde & Bocquet 2018)

$$\int_0^{h/2} (\cosh \Phi - 1)\mathrm{d}z = \frac{2}{\kappa} \left(\sqrt{1 + (1/\kappa \ell_{GC})^2} - 1 \right). \tag{4.15}$$

Here, $\ell_{GC} = (2\pi \ell_B \Sigma_n)^{-1}$ is the Gouy–Chapman length and $\kappa = \sqrt{8\pi \ell_B C_\infty}$ is the inverse Debye length.

To make the gradient term dimensionless, we use $\kappa^2 = 8\pi \ell_B C_\infty$:

$$\frac{\mathrm{d}C_\infty}{\mathrm{d}x} = C_\infty \frac{\mathrm{d}\ln C_\infty}{\mathrm{d}x} = \frac{\kappa^2(C_\infty)}{8\pi \ell_B} \nabla_x \ln C_\infty. \tag{4.16}$$

Substituting the integral result (4.15) and this gradient transformation back into (4.14) yields the final expression for the diffusio-osmotic slip velocity:

$$u_{slip} = \frac{k_B T}{2\pi \eta \ell_B} \frac{b}{\lambda_D} \left[\sqrt{1 + \left(\frac{1}{\kappa \ell_{GC}} \right)^2} - 1 \right] (-\nabla_x \ln C_\infty). \tag{4.17}$$

4.4. *Current–slip relationship*

Using the diffusio-osmotic velocity profile $u(z)$ derived in § 4.3, we now obtain the analytical expression for the diffusion current at the liquid film. The current results from the advection of the net charge density ($\rho_e = e(C_+ - C_-)$) within the EDL. By integrating the product of charge density and flow velocity across the film thickness, we directly relate the macroscopic measurable current to the microscopic slip length.

According to (4.8), we have obtained the diffusion current I_{LG} at the LG interface as

$$I_{LG} = 2\pi r \int_0^{h/2} e(C_+ - C_-) u(z)\,\mathrm{d}z. \tag{4.18}$$

https://doi.org/10.1017/jfm.2026.11975 Published online by Cambridge University Press

Using the Poisson equation $C_+ - C_- = -(\mathrm{d}^2\Phi/\mathrm{d}z^2)/4\pi\ell_B$ (Andelman 1995), the diffusion current (4.8) can be written as

$$I_{LG} = 2\pi r \frac{e}{4\pi\ell_B}\int_0^{h/2}\left(-\frac{\mathrm{d}^2\Phi}{\mathrm{d}z^2}\right)u(z)\,\mathrm{d}z. \tag{4.19}$$

We then integrate (4.19) twice along the z direction and obtain

$$I_{LG} = \frac{er}{2\ell_B}\left\{\frac{\mathrm{d}\Phi}{\mathrm{d}z}(0)u(0) - \Phi(0)\frac{\mathrm{d}u}{\mathrm{d}z}(0) - \int_0^{h/2}\Phi(z)\,[\cosh\Phi(z)-1]\;\mathrm{d}z \times \frac{2k_BT}{\eta}\frac{\mathrm{d}C_\infty}{\mathrm{d}x}\right\}, \tag{4.20}$$

where $u(0) = u_{slip}$ is the slip velocity at the LG interface given by (4.17). In a thin-Debye-length limit, we have $\mathrm{d}z = -\mathrm{d}\Phi/(\kappa\sqrt{2[\cosh\Phi(z)-1]})$ according to Mouterde & Bocquet (2018).

From (4.12), the Stokes equation is also used to calculate the shear rate at the LG surface:

$$\frac{\mathrm{d}u}{\mathrm{d}z}(z=0) = -\frac{2k_BT}{\eta}\int_0^{h/2}[\cosh\Phi(z)-1]\;\mathrm{d}z \times \frac{\mathrm{d}C_\infty}{\mathrm{d}x}. \tag{4.21}$$

Combining the slip velocity (4.17) and the relation $\Sigma_{LG} = -e\Sigma_n$, we derive the diffusion current. To rigorously justify the relative gradient term in (4.23), we apply the dimensional transformation established in (4.16):

$$\frac{\mathrm{d}C_\infty}{\mathrm{d}x} = \frac{\kappa^2(C_\infty)}{8\pi\ell_B}\nabla_x \ln C_\infty. \tag{4.22}$$

Substituting this relation into the integrated current expression effectively normalises the osmotic driving force by the local electrostatic length scales. Consequently, the final expression for the diffusion current is obtained as

$$I_{LG} = 2\pi r(-\Sigma_{LG})\frac{k_BT}{2\pi\eta\ell_B}\left[\frac{b}{\lambda_D}\left(\sqrt{1+\left(\frac{1}{\kappa\ell_{GC}}\right)^2}-1\right)+\left(1-\kappa\ell_{GC}\sinh^{-1}\frac{1}{\kappa\ell_{GC}}\right)\right](-\nabla_x \ln C_\infty). \tag{4.23}$$

In our experiments, $\ell_{GC} \ll \lambda_D$ and the second term in (4.23) can be neglected. The axial salt concentration is described by the steady one-dimensional advection–diffusion profile introduced above. Integrating the logarithmic driving term along the film axis gives $\int_0^L -\nabla_x \ln C_\infty(x)\,\mathrm{d}x = \Delta \ln C_\infty$, where $\Delta \ln C_\infty = \ln(C_{max}/C_{min})$. The corresponding average logarithmic gradient is therefore $\Delta \ln C_\infty/L$. The diffusion current at the LG interface can therefore be written in the reduced form

$$I_{LG} \approx \frac{2\pi r(-\Sigma_{LG})}{L}\frac{k_BT}{2\pi\eta\ell_B}\left[\frac{b}{\lambda_D}\left(\sqrt{1+\left(\frac{1}{\kappa\ell_{GC}}\right)^2}-1\right)+1\right]\Delta\ln(C_\infty). \tag{4.24}$$

For the SL interface, we take no-slip boundary conditions, and their contribution to the diffusion current becomes (Siria *et al.* 2013)

$$I_{SL} \approx \frac{2\pi r(-\Sigma_{SL})}{L}\frac{k_BT}{2\pi\eta\ell_B}\Delta\ln(C_\infty), \tag{4.25}$$

where Σ_{SL} is the surface charge density of the SL interface.

https://doi.org/10.1017/jfm.2026.11975 Published online by Cambridge University Press

Therefore, the diffusion current in the liquid film considering the LG interface (I_{LG}) and SL interface (I_{SL}) of the bubble becomes

$$I_{sys} = -\frac{2\pi r}{L}\frac{k_B T}{2\pi\eta\ell_B}\Sigma_{eff}\Delta\ln(C_\infty), \tag{4.26}$$

where Σ_{eff} is the effective surface charge density considering the diffusion current contributed from the LG and SL interfaces.

Here we introduce an effective surface charge density of the system, considering the non-slip SL and slipping LG interfaces:

$$\Sigma_{eff} = \Sigma_{SL} + \Sigma_{LG}\left[\frac{b}{\lambda_D}\left(\sqrt{1+\left(\frac{1}{\kappa\ell_{GC}}\right)^2}-1\right)+1\right]. \tag{4.27}$$

As seen from (4.27), the effective surface potential (or surface charge density) can be enhanced with a boundary slip.

4.5. *Slip length*

To decouple the contributions of the two interfaces, we first recognise that the surface charge density at the SL interface Σ_{SL} is associated with a no-slip boundary, and therefore independent of the slip length. This value is measured independently via streaming current experiments (see Appendix A). By subtracting this known Σ_{SL} from the total system charge Σ_{eff} (4.27), we isolate the effective surface charge density at the LG interface, which explicitly relates to the slip length b as

$$\Sigma_{LG}^{eff} = \Sigma_{LG}\left[\frac{b}{\lambda_D}\left(\sqrt{1+\left(\frac{1}{\kappa\ell_{GC}}\right)^2}-1\right)+1\right]. \tag{4.28}$$

To estimate Σ_{LG}, we consider the surfactant adsorption dynamics at the LG interface. The adsorption of SDS is typically described by the Frumkin isotherm, which accounts for lateral interactions between adsorbed molecules (Prosser & Franses 2001). However, given the low surfactant concentration in our experiments ($C_{SDS} \leqslant 1$ mM), the system operates in the dilute regime, where the Frumkin isotherm simplifies to the linear Henry adsorption isotherm (Sundin & Bagheri 2022):

$$S = k_d\Gamma_\infty\left(C_k\frac{C_{sur}}{C_{SDS}} - \frac{\Gamma}{\Gamma_\infty}\right), \tag{4.29}$$

where S is the adsorption–desorption flux of surfactants at the LG interface. Parameters C_{sur} and Γ are the bulk surfactant concentration within the liquid film and the surface surfactant concentration adsorbed at the LG interface.

The dimensionless bulk surfactant concentration $C_k = k_a C_{SDS}/k_d$ indicates the surfactant concentration at the LG interface under the adsorption–desorption equilibrium, where k_a is the adsorption coefficient and k_d is the desorption coefficient. Based on the experimental parameters compiled by Prosser & Franses (2001), we adopt the low-salinity limit values to approximate our 1 mM NaCl background. Specifically, we use $k_a/k_d = 0.179\ \mathrm{m^3\ mol^{-1}}$ and the maximum concentration of SDS adsorbed at the LG interface is $\Gamma_\infty = 1/(2.551\times10^5)\ \mathrm{mol\,m^{-2}}$. In this dilute regime, the fraction of bound counterions is negligible (Joly *et al.* 2014), allowing us to assume that the adsorbed surfactant monolayer is fully dissociated.

At equilibrium state, where the amount of surfactant adsorbed and desorbed at the LG surface is balanced ($S \approx 0$), the surfactant concentration within the liquid film equals the

https://doi.org/10.1017/jfm.2026.11975 Published online by Cambridge University Press

bulk surfactant concentration in electrolyte solution ($C_{sur} \approx C_{SDS}$). Substituting $S = 0$ and $C_{sur} \approx C_{SDS}$ into (4.29) yields the surface surfactant concentration at the LG interface, $\Gamma = k_a \Gamma_\infty C_{SDS}/k_d$. Thus, the surface charge density at the LG interface Σ_{LG} becomes

$$\Sigma_{LG} = \frac{eN_A k_a \Gamma_\infty C_{SDS}}{k_d} + \Sigma_0, \tag{4.30}$$

where N_A is the Avogadro constant and $\Sigma_0 = 0.003716\ \mathrm{C\,m^{-2}}$ is the surface charge density of the pure LG interface (Ma *et al.* 2020). Using (4.28), the slip length b can be expressed as

$$b = \frac{\lambda_D(\Sigma_{LG}^{eff}/\Sigma_{LG} - 1)}{\sqrt{1 + (1/\kappa \ell_{GC})^2} - 1}. \tag{4.31}$$

Equation (4.31) quantitatively describes the relationship between slip length and surface charge density, enabling us to characterise the hydrodynamic slip via enhanced surface potential and electrokinetic phenomena.

5. Experimental results

5.1. *Derivation of effective surface charge density*

According to (4.26), the normalised diffusion current $I_{sys}L$ is proportional to the osmotic pressure ($\sim RT\ \ln(C_{max}/C_{min})$) in various SDS concentrations, as observed in figure 3(*a*). The addition of SDS surfactant significantly enhances the diffusion current within the bubble liquid film when $C_{SDS} \leqslant 1$ mM, which we attributed to the joint actions of adsorbed surfactants and the slip length at the LG interface.

To quantify these effects, we determine the effective surface charge density of the liquid film system, Σ_{eff}, which includes contributions from both LG and SL interfaces. Following (4.26), Σ_{eff} is extracted from the slopes of the linear fits in figure 3(*a*). The results are shown as blue circles in figure 3(*b*), with error bars given by the standard deviation of the linear fitting. The effective surface charge density Σ_{eff} varies non-monotonically with surfactant concentration. Here Σ_{eff} increases with C_{SDS}, reaches a maximum near $C_{SDS} \approx 10^{-1}$ mM and then decreases at higher concentrations.

To separate the contribution from the SL interface, we performed streaming current measurements (Delgado *et al.* 2007) in a glass capillary without a bubble using 1 mM NaCl solutions at different SDS concentrations (Appendix A). The derived Σ_{SL} values (green circles) remain nearly constant at all surfactant concentrations, as shown in figure 3(*b*). The constant zeta potential at the SL surface could be understood as the intrinsic surface charge density of the glass surface (pH = 9), while adsorption of SDS has a limited contribution.

With the characterised Σ_{SL}, we can derive an effective surface charge density at the LG interface Σ_{LG}^{eff} from (4.27). The resulting Σ_{LG}^{eff} (red circles in figure 4*a*) is much larger than Σ_{SL}, due to the joint action of adsorbed ionic surfactants and boundary slip. Equation (4.28) describes the amplifications by hydrodynamic slip by a factor of b/λ_D.

As C_{SDS} increases, we found that Σ_{LG}^{eff} initially rises, consistent with the quantity of anionic surfactants adsorbed at the LG interface. When $C_{SDS} > 10^{-1}$ mM, Σ_{LG}^{eff} begins to plateau and eventually decreases. We attribute this non-monotonic trend to a reduction in slip length caused by surfactant adsorption at the LG interface. At sufficiently high SDS concentrations, the adsorbed layer becomes less mobile and increases interfacial friction, which suppresses slip and weakens the slip-amplification effect. At $C_{SDS} = 1$ mM, the slip

https://doi.org/10.1017/jfm.2026.11975 Published online by Cambridge University Press

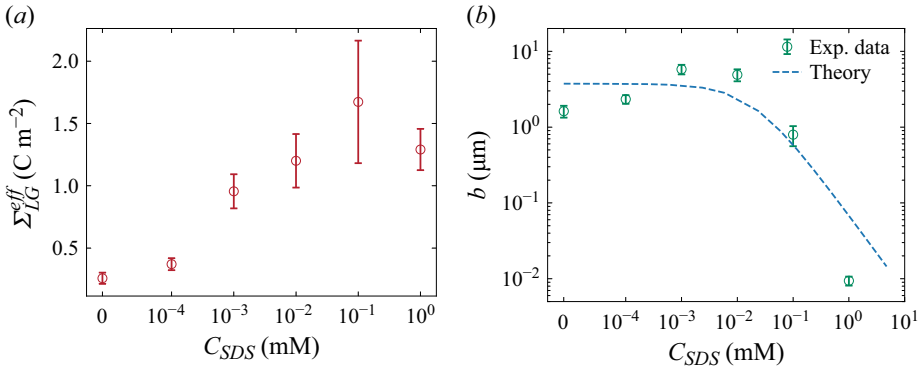


Figure 4. (*a*) Measured the effective surface charge density Σ_{LG}^{eff} (red circles) versus SDS concentration C_{SDS} at 1 mM NaCl. (*b*) Interfacial slip length as a function of C_{SDS}, demonstrating suppression at $C_{SDS} \geqslant 10^{-2}$ mM due to interfacial immobilisation.

length is strongly reduced, approaching a no-slip limit, and Σ_{LG}^{eff} decreases despite the higher surfactant coverage.

5.2. *Derivation of slip length at the LG interface*

With the isolated zeta potential at the LG interface, we could derive the intrinsic slip length at the LG interface as a function of surfactant concentration by using (4.31). The green circles in figure 4(*b*) represent the derived slip length from the measured zeta potential, and the dashed lines are the theoretical predictions that were developed in this work based on our previous theoretical framework (Yan *et al.* 2025) as shown in Appendix B.

When the surfactant concentration is lower than 10^{-2} mM, the slip length remains nearly constant, approaching 3 μm as the intrinsic slip length at the LG interface. Our results indicate that a small amount of SDS surfactant will not clearly reduce the slip length, which is in agreement with theoretical predictions (Peaudecerf *et al.* 2017; Landel *et al.* 2020; Yan *et al.* 2025). However, when the surfactant concentration exceeds 10^{-2} mM, the slip length rapidly decreases, dropping by nearly two orders of magnitude at 1 mM. This dramatic reduction of slip length explains the decrease of zeta potential when surfactant concentration exceeds 10^{-1} mM in figure 4(*a*).

Based on the theoretical model, the reduction in slip length can be attributed to the joint actions of surfactant adsorption and Marangoni stresses. At low surfactant concentrations ($C_{SDS} < 10^{-2}$ mM), adsorption–desorption processes at the LG interface are relatively balanced, resulting in small interfacial concentration gradients and negligible Marangoni stresses. Under such conditions, the slip length is governed primarily by the intrinsic interfacial friction of a clean surface. In contrast, at higher concentrations ($C_{SDS} > 10^{-2}$ mM), surfactant adsorption increases markedly, amplifying the interfacial concentration gradient and enhancing Marangoni stresses. The associated rise in interfacial stress significantly reduces the slip length, which approaches a no-slip condition when C_{SDS} exceeds 1 mM. Thus, we could conclude that the zeta potential at surfactant-covered bubble film increases when $C_{SDS} < 10^{-1}$ mM since the adsorbed SDS increases the charge density at the LG interface. However, the highly packed SDS molecules result in a significant increase of the friction coefficient at the LG interface, thus suppressing the slip length and zeta potential, as evident from both experimental and theoretical results.

The strongly enhanced effective surface charge density may significantly increase the electrokinetic phenomena and performance of potential applications like osmotic energy

https://doi.org/10.1017/jfm.2026.11975 Published online by Cambridge University Press

harvesting (Xu *et al.* 2024). We gained electricity via net diffusion current across the bubble under osmotic pressure. The osmotic power is proportional to the square of effective surface charge density of nanochannels $P_{max} = I_{sys}^2/4G_f \propto \Sigma_{eff}^2$ (Ren & Stein 2008; Siria *et al.* 2013).

In conventional solid nanochannels, the surface potential is typically of the order of tens of millivolts under no-slip boundary conditions. However, owing to interfacial slip at the LG interface, the zeta potential may be significantly enhanced to ~ 100 mV range, due to the adsorption of ionic surfactant and boundary slip. Thus, the figure of merit in osmotic energy conversion can be enhanced by an order of magnitude, while the power generation was enhanced by 2–3 orders of magnitude.

However, since the non-conductive gas bubble occupies most of the area of the microchannel, the power density is strongly limited. But, if it is possible to work with foams or bubble lattices, which have a large surface-to-volume ratio of LG interface, it will be helpful to enhance the power density. Overall, the liquid-film nanochannel framework provides a route to use soft, slipping interfaces to enhance mass transport at the nanoscale.

6. Conclusion

In this work, we investigated the diffusion current, a family of electrokinetic phenomena, across a bubble interface, where a thin liquid film forms at the interface between a gas bubble and a cylindrical glass capillary. We first measured the diffusion current and film conductance, from which the film thickness was determined. Our results showed that the diffusion current increases with the osmotic pressure, allowing us to derive an effective zeta potential of the bubble film system. The presence of surfactants strongly increases the diffusion current and effective surface charge density at the LG interface, due to the enhanced surface charge density by ionic-surfactant adsorption at the LG interface, and reaches a peak value at 10^{-1} mM. However, the effective surface charge density starts to decrease once the surfactant concentration exceeds a threshold value, which we attribute to a reduction in the slip length.

To explain this behaviour, we formulated an analytical theory based on isotherm adsorption and Marangoni stress of adsorbed surfactants, to describe the surfactant-induced change of slip length at the LG interface. Our theory can well describe the diffusion current with a slip boundary under osmotic pressure, which helps to derive the slip length at the LG interface as a function of surfactant concentration. Our calculation from experimental results showed that the slip length at the LG interface remains nearly constant (3 μm) when SDS concentration is below 10^{-2} mM. However, it dramatically decreases when C_{SDS} exceeds 10^{-2} mM due to the joint actions of increased surfactant adsorption and Marangoni stress. Both effects increase the friction of LG interfaces, decreasing the slip length at 1 mM SDS and approaching a no-slip condition. We demonstrate that boundary slip at the LG interface can reinforce osmotic power harvesting compared with no-slip systems. Our findings provide new insights into the electrokinetic and transport behaviour at solid–liquid–gas interfaces, offering a quantitative framework for understanding mass transport and interfacial slip under electric field effects.

Funding. This work is supported by the National Natural Science Foundation of China under grant nos. 12388101 and 12550001 and the Innovation Capability Support Program of Shaanxi under grant no. 2024RS-CXTD-15.

Declaration of interests. The authors report no conflict of interest.

https://doi.org/10.1017/jfm.2026.11975 Published online by Cambridge University Press

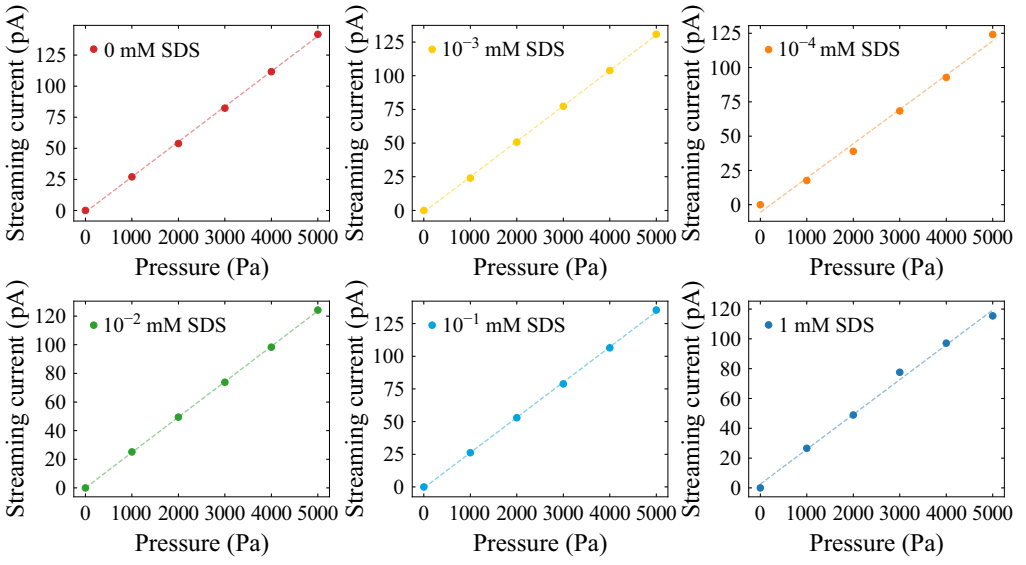


Figure 5. The streaming current exhibits a linear increase with the external pressure difference across a range of SDS concentrations.

Appendix A. Zeta potential at the solid–liquid interface

We determine the zeta potential at the SL interface by measuring the streaming current in a glass capillary. When an external pressure difference Δp is applied across the capillary, it induces fluid flow, which mobilises counterions in the EDL, generating a streaming current I_{str}. This current is related to the zeta potential ζ_{SL} by the expression

$$I_{str} = -\frac{\varepsilon_0 \varepsilon_r \pi r_c^2}{\eta} \frac{\Delta p}{L_c} \zeta_{SL}, \tag{A1}$$

where $r_c = 50\ \mu\text{m}$ is the capillary radius and $L_c = 1.5$ cm is the capillary length.

To investigate the effect of surfactants, we use a Fluigent pressure pump to drive a 1 mM NaCl solution through the capillary while maintaining a fixed pH of 9. Ag/AgCl electrodes at both ends of the capillary, connected to a Keithley 6430 source meter, continuously record the streaming current. The SDS concentration is systematically varied from 0 to 1 mM while keeping the NaCl concentration constant at 1 mM. Figure 5 shows a linear relationship between streaming current and applied pressure difference for different SDS concentrations. By fitting the data to (A1), we extract the zeta potential ζ_{SL} at the SL interface as a function of surfactant concentration. Based on the Gouy–Chapman theory, the corresponding surface charge density at the SL interface was calculated using the Grahame relation (Baldessari 2008):

$$\Sigma_{SL} = \frac{2\pi \ell_B \lambda_D}{e} \sinh\left(\frac{e\zeta_{SL}}{2k_B T}\right). \tag{A2}$$

Appendix B. Slip length

To evaluate the boundary slip at the LG interface, we first calculate the friction coefficient of surfactants adsorbed at the interface. A single negatively charged surfactant molecule

https://doi.org/10.1017/jfm.2026.11975 Published online by Cambridge University Press

at the LG interface experiences friction due to the shear stress of surrounding water (first term in (B1)) and Marangoni effects (second term in (B1)). At steady state, the force on a single surfactant is balanced as

$$\lambda_s \left(u_{slip} - u_i\right) - \frac{1}{N_A}\frac{\mathrm{d}\mu}{\mathrm{d}x} = 0. \tag{B1}$$

Here, $\lambda_s = 3\pi\eta r_d$ represents the friction coefficient between surfactants and the surrounding liquid (Joly *et al.* 2014), where r_d denotes the hydration radius of the surfactant hydrophilic head. Parameter u_i is the velocity of a single surfactant adsorbed at the LG interface. The term $\mathrm{d}\mu/\mathrm{d}x$ indicates the chemical potential gradient induced by non-uniform surfactant distribution. Consequently, solving (B1) gives the surfactant velocity:

$$u_i = u_{slip} - \frac{1}{\lambda_s N_A}\frac{\mathrm{d}\mu}{\mathrm{d}x}. \tag{B2}$$

To obtain a modified slip boundary condition in the presence of Marangoni stress, we consider the force balance on the interfacial fluid layer, consisting of the liquid and surfactants adsorbed at the LG interface as follows:

$$\eta\frac{\mathrm{d}U}{\mathrm{d}z}\bigg|_{z=0} - \lambda_s \Gamma N_A (u_{slip} - u_i) - \lambda_0 u_{slip} = 0. \tag{B3}$$

Here, U is the flow velocity within the liquid film, λ_0 is the friction coefficient between the liquid and a clean LG interface and Γ is the surface surfactant concentration at the LG interface.

We next model the transport of surfactants along the LG interface. Surfactant accumulation downstream and depletion upstream lead to a surface tension gradient, which drives Marangoni stress. Since the liquid film thickness h is far smaller than the bubble length L, we derive a one-dimensional convection–diffusion equation for surfactants at the LG interface as

$$\frac{\partial\left(u_i \Gamma\right)}{\partial x} = D\frac{\partial^2 \Gamma}{\partial x^2} + S, \tag{B4}$$

where $D = 7.0 \times 10^{-10}\ \mathrm{m^2\ s^{-1}}$ represents the diffusion coefficient of SDS surfactants, based on Peaudecerf *et al.* (2017) and S is the source term, indicating adsorption and desorption fluxes of surfactants at the LG interface.

The normal diffusive flux from the bulk to the interface is balanced by S as follows:

$$D\frac{\partial c}{\partial z}|_{z=0} = S. \tag{B5}$$

Assuming a linear variation in surfactant concentration along the interface and uniform distribution at the bubble meniscus, we simplify the Frumkin adsorption isotherm to the Henry isotherm (Landel *et al.* 2020), leading to a linearised form of S:

$$S = k_d \Gamma_\infty \left(C_k C_{sur}/C_{SDS} - \theta\right), \tag{B6}$$

where $C_k = k_a C_{SDS}/k_d$ is the dimensionless bulk surfactant concentration, C_{sur} is the bulk surfactant concentration near the LG interface and $\theta = \Gamma/\Gamma_\infty$ is the dimensionless surface surfactant concentration at the LG interface, representing surfactant coverage. Utilising the linearised source term S, we approximate $\theta = C_k$ at $x = 0$.

https://doi.org/10.1017/jfm.2026.11975 Published online by Cambridge University Press

According to (B4)–(B6), and referring to the derivation process of Yan *et al.* (2025), we can obtain the surfactant reduction upstream of the bubble $\Delta\theta$:

$$\Delta\theta = \frac{u_{slip} C_k}{\dfrac{2D}{L} + \dfrac{Lk_d}{4(1 + k_a \Gamma_\infty h/D)} + \dfrac{2nRT}{N_A L \lambda_s}}. \tag{B7}$$

The linearised Marangoni stress f_M is related to this depletion $\Delta\theta$ as

$$f_M = -nRT\Gamma_\infty \frac{2\Delta\theta}{L}, \tag{B8}$$

where n is the surfactant style constant.

From (B7) and (B8), the chemical potential gradient $\mathrm{d}\mu/\mathrm{d}x$ is expressed as

$$\frac{\mathrm{d}\mu}{\mathrm{d}x} = -\frac{f_M}{C_k \Gamma_\infty} = \frac{\alpha_s u_{slip}}{C_k \Gamma_\infty}, \tag{B9}$$

where the parameter $\alpha_s = 2nRT\Gamma_\infty C_k/(2D + (L^2 k_d/(4(1 + k_a \Gamma_\infty h/D))) + 2nRT/N_A \lambda_s)$ quantifies the strength of the Marangoni effect.

To estimate the slip length at the surfactant-covered LG interface, we derived the friction coefficient, given by $f = \lambda(u_{slip} - u_i)$. Here, f is the stress borne by surfactants at the LG interface, which is equal to the negative value of the Newtonian shear stress, and λ is the effective friction coefficient between liquid and gas considering viscous stress, electrostatic force and the Marangoni stress. Therefore, using (B1) and (B3), the total friction coefficient becomes

$$\lambda = \lambda_s \Gamma N_A + \frac{\lambda_0 \lambda_s N_A \Gamma_\infty C_k}{\alpha_s}. \tag{B10}$$

The slip length can be derived by the Navier boundary condition $b = \eta/\lambda$ as

$$b = \frac{2nRT\eta}{2nRT\lambda_s \Gamma_\infty N_A C_k + \lambda_0 \lambda_s N_A \left[2D + \dfrac{L^2 k_d}{4(1 + k_a \Gamma_\infty h/D)} + \dfrac{2nRT}{N_A \lambda_s}\right]}. \tag{B11}$$

Equation (B11) shows that the slip length b depends on the surfactant concentration. It can be observed that the slip length b is related to the surfactant concentration. As the surfactant concentration approaches zero, the slip length tends towards a constant value corresponding to the clean interface. With increasing surfactant concentration, the slip length decreases and exhibits an inverse relationship, highlighting the dominant role of Marangoni-induced resistance.

https://doi.org/10.1017/jfm.2026.11975 Published online by Cambridge University Press

Appendix C. Variables

Parameter	Symbol	Value	Unit
Ion mobility	μ	5.19×10^{-8}	$m^2\ s^{-1}\ V^{-1}$
Bjerrum length	ℓ_B	0.7	nm
Elementary charge	e	1.6×10^{-19}	C
Liquid viscosity	η	1.01×10^{-3}	Pa s
Interfacial tension	γ	7.2×10^{-2}	$N\ m^{-1}$
Hamaker constant	A	-1.03×10^{-20}	J
Boltzmann constant	k_B	1.38×10^{-23}	$J\ K^{-1}$
Temperature	T	295.15	K
Vacuum permittivity	ε_0	8.85×10^{-12}	$F\ m^{-1}$
Relative permittivity of liquid	ε_r	78	1
Surfactant style constant	n	2	1
Gas constant	R	8.314	$J\ K^{-1}\ mol^{-1}$
Contact angle	α	15	(deg.)

Table 1. Physical constants.

C (mM)	k_b ($S\ m^{-1}$)
1	0.01481
10	0.1218
20	0.2369
50	0.5622
100	1.088
200	2.056

Table 2. Measured bulk conductivity of NaCl solutions used for calibration $k_b(C)$.

C_{SDS} (mM)	$\frac{C_{max}}{C_{min}} = 10$	$\frac{C_{max}}{C_{min}} = 20$	$\frac{C_{max}}{C_{min}} = 50$	$\frac{C_{max}}{C_{min}} = 100$	$\frac{C_{max}}{C_{min}} = 200$
0	0.57	0.52	0.98	1.05	1.25
10^{-4}	0.22	0.37	0.74	0.84	0.92
10^{-3}	0.05	0.13	0.34	0.47	0.83
10^{-2}	0.10	0.17	0.32	0.52	0.88
10^{-1}	0.08	0.22	0.27	0.41	0.94
1	0.17	0.21	0.49	0.62	0.92

Table 3. Calculated Péclet numbers Pe for different surfactant concentrations C_{SDS} and salinity gradients C_{max}/C_{min}.

https://doi.org/10.1017/jfm.2026.11975 Published online by Cambridge University Press

C (mM)	ζ_{LG} (mV)	ζ_{SL} (mV)
0.01	−117	−57.0
0.1	−115	−42.1
1	−94.3	−28.9
10	−65.0	−27.4
100	−35.9	−17.3

Table 4. Measured zeta potentials at the solid–liquid (ζ_{SL}) and liquid–gas (ζ_{LG}) interfaces in various surfactant-free NaCl concentrations (Ma *et al.* 2020).

References

An, H., Liu, G. & Craig, V.S.J. 2015 Wetting of nanophases: nanobubbles, nanodroplets and micropancakes on hydrophobic surfaces. *Adv. Colloid Interface Sci.* **222**, 9–17.

Andelman, D. 1995 Electrostatic properties of membranes: the Poisson–Boltzmann theory. In *Handbook of Biological Physics* (ed. R. Lipowsky & E. Sackmann), vol. 1, pp. 603–642. Elsevier.

Aurelian, F., Patrick, M., Mohamed, H. 2011 Wall slip effects in (elasto) hydrodynamic journal bearings. *Tribol. Intl* **44** (7–8), 868–877.

Baldessari, F. 2008 Electrokinetics in nanochannels. *J. Colloid Interface Sci.* **325** (2), 526–538.

Berkelaar, R.P., Zandvliet, H.J.W. & Lohse, D. 2013 Covering surface nanobubbles with a NaCl nanoblanket. *Langmuir* **29** (36), 11337–11343.

Bobji, M.S., Kumar, S.V., Asthana, A. & Govardhan, R.N. 2009 Underwater sustainability of the 'cassie' state of wetting. *Langmuir* **25** (20), 12120–12126.

Bouzigues, C.I., Tabeling, P. & Bocquet, L. 2008 Nanofluidics in the debye layer at hydrophilic and hydrophobic surfaces. *Phys. Rev. Lett.* **101** (11), 114503.

Cai, X., Li, X. & Bian, X. 2025 Dynamics of an elliptical cylinder in confined poiseuille flow under navier slip boundary conditions. *Acta Mechanica Sin.* **41** (8), 725236.

Choi, C.-H. & Kim, C.-J. 2006 Large slip of aqueous liquid flow over a nanoengineered superhydrophobic surface. *Phys. Rev. Lett.* **96** (6), 066001.

Choi, C.-H., Ulmanella, U., Kim, J., Ho, C.-M. & Kim, C.-J. 2006 Effective slip and friction reduction in nanograted superhydrophobic microchannels. *Phys. Fluids* **18** (8), 087105.

Davies, J., Maynes, D., Webb, B.W. & Woolford, B. 2006 Laminar flow in a microchannel with superhydrophobic walls exhibiting transverse ribs. *Phys. Fluids* **18** (8), 087110.

Delgado, A.V., González-Caballero, F., Hunter, R.J., Koopal, L.K. & Lyklema, J. 2007 Measurement and interpretation of electrokinetic phenomena. *J. Colloid Interface Sci.* **309** (2), 194–224.

Fair, J.C. & Osterle, J.F. 1971 Reverse electrodialysis in charged capillary membranes. *J. Chem. Phys.* **54** (8), 3307–3316.

Feuillebois, F., Bazant, M.Z. & Vinogradova, O.I. 2009 Effective slip over superhydrophobic surfaces in thin channels. *Phys. Rev. Lett.* **102** (2), 026001.

Haase, A.S., Wood, J.A., Lammertink, R.G.H. & Snoeijer, J.H. 2016 Why bumpy is better: the role of the dissipation distribution in slip flow over a bubble mattress. *Phys. Rev. Fluids* **1** (5), 054101.

Hough, D.B. & White, L.R. 1980 The calculation of hamaker constants from liftshitz theory with applications to wetting phenomena. *Adv. Colloid Interface Sci.* **14** (1), 3–41.

Hu, H., Wang, D., Ren, F., Bao, L., Priezjev, N.V. & Wen, J. 2018 A comparative analysis of the effective and local slip lengths for liquid flows over a trapped nanobubble. *Intl J. Multiphase Flow* **104**, 166–173.

Huang, S., Lv, P. & Duan, H. 2019 Morphology evolution of liquid–gas interface on submerged solid structured surfaces. *Extreme Mech. Lett.* **27**, 34–51.

Huang, D.M., Sendner, C., Horinek, D., Netz, R.R. & Bocquet, L. 2008 Water slippage versus contact angle: a quasiuniversal relationship. *Phys. Rev. Lett.* **101** (22), 226101.

Joly, L., Detcheverry, F.çois & Biance, A.-L. 2014 Anomalous ζ potential in foam films. *Phys. Rev. Lett.* **113** (8), 088301.

Karatay, E., Haase, A.S., Visser, C.W., Sun, C., Lohse, D., Tsai, P.A. & Lammertink, R.G.H. 2013 Control of slippage with tunable bubble mattresses. *Proc. Natl Acad. Sci.* **110** (21), 8422–8426.

Landel, J.R., Peaudecerf, F.J., Temprano-Coleto, F., Gibou, F., Goldstein, R.E. & Luzzatto-Fegiz, P. 2020 A theory for the slip and drag of superhydrophobic surfaces with surfactant. *J. Fluid Mech.* **883**, A18.

Lauga, E. & Stone, H.A. 2003 Effective slip in pressure-driven Stokes flow. *J. Fluid Mech.* **489**, 55–77.

https://doi.org/10.1017/jfm.2026.11975 Published online by Cambridge University Press

LEE, T., CHARRAULT, E. & NETO, C. 2014*b* Interfacial slip on rough, patterned and soft surfaces: a review of experiments and simulations. *Adv. Colloid Interface* **210**, 21–38.
LEE, C., CHOI, C.-H. & KIM, C.J. 2008 Structured surfaces for a giant liquid slip. *Phys. Rev. Lett.* **101** (6), 064501.
LEE, C., CHOI, C.-H. & KIM, C.-J. 2016 Superhydrophobic drag reduction in laminar flows: a critical review. *Exp. Fluids* **57** (12), 176.
LEE, C., COTTIN-BIZONNE, C., BIANCE, A.-L., JOSEPH, P., BOCQUET, L. & YBERT, C. 2014*a* Osmotic flow through fully permeable nanochannels. *Phys. Rev. Lett.* **112** (24), 244501.
LEE, A. & KIM, H.-Y. 2014 Does liquid slippage within a rough channel always increase the flow rate? *Phys. Fluids* **26** (7), 072002.
LEVINE, S., MARRIOTT, J.R. & ROBINSON, K. 1975 Theory of electrokinetic flow in a narrow parallel-plate channel. *J. Chem. Soc. Faraday Trans. 2* **71**, 1.
LI, B., *et al.* 2025 Bipolar nanofluidic channel: from rectifier to capacitor. *Acta Mechanica Sin.* **41** (8), 725161.
LI, Z., JI, S., DUAN, H., LAN, S., ZHANG, J. & LV, P. 2020*b* Coupling effect of wall slip and spanwise oscillation on drag reduction in turbulent channel flow. *Phys. Rev. Fluids* **5** (12), 124601.
LI, D., JING, D., PAN, Y., BHUSHAN, B. & ZHAO, X. 2016 Study of the relationship between boundary slip and nanobubbles on a smooth hydrophobic surface. *Langmuir* **32** (43), 11287–11294.
LI, H., LI, Z., TAN, X., WANG, X., HUANG, S., XIANG, Y., LV, P. & DUAN, H. 2020*a* Three-dimensional backflow at liquid–gas interface induced by surfactant. *J. Fluid Mech.* **899**, A8.
LIU, G. & CRAIG, V.S.J. 2009 Improved cleaning of hydrophilic protein-coated surfaces using the combination of nanobubbles and SDS. *ACS Appl. Mater. Interfaces* **1** (2), 481–487.
LOHSE, D. & ZHANG, X. 2015 Surface nanobubbles and nanodroplets. *Rev. Mod. Phys.* **87** (3), 981–1035.
LONG, R., ZHAO, Y., KUANG, Z., LIU, Z. & LIU, W. 2020 Hydrodynamic slip enhanced nanofluidic reverse electrodialysis for salinity gradient energy harvesting. *Desalination* **477**, 114263.
LV, P., XUE, Y. & DUAN, H. 2016 Stability and evolution of liquid–gas interfaces on superhydrophobic surfaces. *Adv. Mech.* **46** (201604), 201604.
LV, P., XUE, Y., SHI, Y., LIN, H. & DUAN, H. 2014 Metastable states and wetting transition of submerged superhydrophobic structures. *Phys. Rev. Lett.* **112** (19), 196101.
MA, Y., SUN, M., DUAN, X., VAN DEN, B., ALBERT, E., JAN, C.T. & XIE, Y. 2020 Dimension-reconfigurable bubble film nanochannel for wetting based sensing. *Nat. Commun.* **11** (1), 814.
MING, Z., JIAN, L., CHUNXIA, W., XIAOKANG, Z. & LAN, C. 2011 Fluid drag reduction on superhydrophobic surfaces coated with carbon nanotube forests (CNTs). *Soft Matt.* **7** (9), 4391.
MOUTERDE, T.ÉE & BOCQUET, L.ÉRIC 2018 Interfacial transport with mobile surface charges and consequences for ionic transport in carbon nanotubes. *Eur. Phys. J. E* **41** (12), 148.
NAJAFI, A.S., DRELICH, J., YEUNG, A., XU, Z. & MASLIYAH, J. 2007 A novel method of measuring electrophoretic mobility of gas bubbles. *J. Colloid Interface Sci.* **308** (2), 344–350.
NAVIER, C. 1822 *Mémoire sur les lois du Mouvement des Fluides*. Éditeur Inconnu.
NIU, Y., MA, Y. & XIE, Y. 2024 Soft memristor at a microbubble interface. *Nano Lett.* **24** (34), 10475–10481.
NIU, Y. & XIE, Y. 2025 Electrohydrodynamics of ionic-surfactant-covered liquid films in soft memristors. *Phys. Rev. Fluids* **10** (9), 093702.
NIZKAYA, T.V., DUBOV, A.L., MOURRAN, A. & VINOGRADOVA, O.I. 2016 Probing effective slippage on superhydrophobic stripes by atomic force microscopy. *Soft Matt.* **12** (33), 6910–6917.
OU, J., PEROT, B. & ROTHSTEIN, J.P. 2004 Laminar drag reduction in microchannels using ultrahydrophobic surfaces. *Phys. Fluids* **16** (12), 4635–4643.
PEAUDECERF, F.J., LANDEL, J.R., GOLDSTEIN, R.E. & LUZZATTO-FEGIZ, P. 2017 Traces of surfactants can severely limit the drag reduction of superhydrophobic surfaces. *Proc. Natl Acad. Sci.* **114** (28), 7254–7259.
POETES, R., HOLTZMANN, K., FRANZE, K. & STEINER, U. 2010 Metastable underwater superhydrophobicity. *Phys. Rev. Lett.* **105** (16), 166104.
PRIEVE, D.C., ANDERSON, J.L., EBEL, J.P. & LOWELL, M.E. 1984 Motion of a particle generated by chemical gradients. Part 2. Electrolytes. *J. Fluid Mech.* **148**, 247–269.
PROSSER, A.J. & FRANSES, E.I. 2001 Adsorption and surface tension of ionic surfactants at the air–water interface. *Rev. Evaluat. Equilib. Models* **178** (1–3), 1–40.
QIN, X., YUAN, Q., ZHAO, Y., XIE, S. & LIU, Z. 2011 Measurement of the rate of water translocation through carbon nanotubes. *Nano Lett.* **11** (5), 2173–2177.
RANKIN, D.J. & HUANG, D.M. 2016 The effect of hydrodynamic slip on membrane-based salinity-gradient-driven energy harvesting. *Langmuir* **32** (14), 3420–3432.
REN, Y. & STEIN, D. 2008 Slip-enhanced electrokinetic energy conversion in nanofluidic channels. *ACS Symp. Ser.* **19** (19), 195707.
REYSSAT, M., YEOMANS, J.M. & QUÉRÉ, D. 2008 Impalement of fakir drops. *EPL* **81** (2), 26006.

https://doi.org/10.1017/jfm.2026.11975 Published online by Cambridge University Press

ROTHSTEIN, J.P. 2010 Slip on superhydrophobic surfaces. *Annu. Rev. Fluid Mech.* **42** (1), 89–109.
SCHOCH, R.B., HAN, J. & RENAUD, P. 2008 Transport phenomena in nanofluidics. *Rev. Mod. Phys.* **80** (3), 839–883.
SECCHI, E., MARBACH, S., NIGUÈS, A., STEIN, D., SIRIA, A. & BOCQUET, L. 2016 Massive radius-dependent flow slippage in carbon nanotubes. *Nature* **537** (7619), 210–213.
SEDDON, J.R.T. & LOHSE, D. 2011 Nanobubbles and micropancakes: gaseous domains on immersed substrates. *J. Phys.: Condens. Matter* **23** (13), 133001.
SIRIA, A., PONCHARAL, P., BIANCE, A.-L., FULCRAND, R., BLASE, X., PURCELL, S.T., BOCQUET, L. 2013 Giant osmotic energy conversion measured in a single transmembrane boron nitride nanotube. *Nature* **494** (7438), 455–458.
SPARREBOOM, W., VAN DEN BERG, A. & EIJKEL, J.C.T. 2009 Principles and applications of nanofluidic transport. *Nat. Nanotechnol.* **4** (11), 713–720.
SUNDIN, J. & BAGHERI, S. 2022 Slip of submerged two-dimensional liquid-infused surfaces in the presence of surfactants. *J. Fluid Mech.* **950**, A35.
TRUESDELL, R., MAMMOLI, A., VOROBIEFF, P., VAN SWOL, F. & BRINKER, C.J. 2006 Drag reduction on a patterned superhydrophobic surface. *Phys. Rev. Lett.* **97** (4), 044504.
TSAI, P., LAMMERTINK, R.G.H., WESSLING, M. & LOHSE, D. 2010 Evaporation-triggered wetting transition for water droplets upon hydrophobic microstructures. *Phys. Rev. Lett.* **104** (11), 116102.
TYRRELL, J.W.G. & ATTARD, P. 2001 Images of nanobubbles on hydrophobic surfaces and their interactions. *Phys. Rev. Lett.* **87** (17), 176104.
VERSCHOOF, R.A., VAN DER VEEN, R.C. A., SUN, C. & LOHSE, D. 2016 Bubble drag reduction requires large bubbles. *Phys. Rev. Lett.* **117** (10), 104502.
WANG, Y., BHUSHAN, B. & MAALI, A. 2009 Atomic force microscopy measurement of boundary slip on hydrophilic, hydrophobic, and superhydrophobic surfaces. *J. Vacuum Sci. Technol. A: Vacuum Surfaces Films* **27** (4), 754–760.
WANG, H., WANG, K. & LIU, G. 2022 Drag reduction by gas lubrication with bubbles. *Ocean Engng* **258**, 111833.
WU, C., NESSET, K., MASLIYAH, J. & XU, Z. 2012 Generation and characterization of submicron size bubbles. *Adv. Colloid Interface Sci.* **179–182**, 123–132.
XIA, K.-Q. 2024 Unveiling the mystery of effective slip. *J. Fluid Mech.* **1000**, F5.
XU, D., YAN, M. & XIE, Y. 2024 Energy harvesting from water streaming at charged surface. *Electrophoresis* **45** (3–4), 244–265.
YAN, M., NIU, Y., SUN, M. & XIE, Y. 2025 Onsager relation for electrokinetics at surfactant-covered bubble film. *Droplet* **4** (3), e70007.
YAN, X., SONG, Y., ZHENG, H., CUI, H., WANG, Z. & XU, W. 2024 A bubble energy generator featuring lubricant-impregnated surface with high durability and efficiency. *Nano Energy* **121**, 109238.
ZHANG, X., CHAN, D.Y.C., WANG, D. & MAEDA, N. 2013 Stability of interfacial nanobubbles. *Langmuir* **29** (4), 1017–1023.

https://doi.org/10.1017/jfm.2026.11975 Published online by Cambridge University Press